Current prospects for ASTROD Inertial Sensor

A. PULIDO PATÓN

Center for Gravitation and Cosmology, Purple Mountain Observatory,
Chinese Academy of Sciences, Beijing West Road 2,
Nanjing 210008, China.
antonio@pmo.ac.cn

The Astrodynamical Space Test of Relativity using Optical Devices (ASTROD) is a multi-purpose relativity mission concept. ASTROD's scientific goals are the measurement of relativistic and solar system parameters to unprecedented precision, and the detection and observation of low-frequency gravitational waves to frequencies down to 5×10^{-6} Hz. To accomplish its goals, ASTROD will employ a constellation of drag-free satellites, aiming for a residual acceleration noise of $(0.3\text{-}1) \times 10^{-15}$ m s^{-2} Hz$^{-1/2}$ at 0.1 mHz. Noise sources and strategies for improving present acceleration noise levels are reported.

Keywords: ASTROD; LISA; Space interferometers; Inertial sensors.

1. Introduction

The classical concept of a drag-free satellite[1] consists of a small proof mass inserted inside a large spacecraft. The larger spacecraft shields external forces, allowing the proof mass to move in free fall. The relative position and orientation of the proof mass with respect to the main spacecraft is sensed along its trajectory. This information is feedback to thrusters on the main spacecraft, which are subsequently fired to maintain the proof mass-spacecraft relative position and orientation. In this way, the coupling of external forces to the proof mass is minimized.

Numerous space missions have already employed drag-free technology. The first example of a "drag-free" mission to test fundamental physics is Gravity Probe B (GP-B).[2] GP-B was launched in April 2004 and has experimentally measured frame-dragging and geodetic effects. By spring of 2007, the results of the data analysis will become public. The GP-B inertial sensor achieved a level of free fall below 2×10^{-12} m s^{-2} Hz$^{-1/2}$ at 5×10^{-3} Hz.

The Laser Interferometer Space Antenna, LISA, is another fundamental physics mission requiring drag-free performance. The LISA mission concept[3] consists of three spacecraft in heliocentric orbits, forming a nearly equilateral triangle formation of side 5×10^6 km and inclined with respect to the ecliptic by 60°. LISA will monitor the separation between free falling proof masses, which are shielded within the spacecraft, by using interferometric techniques, to detect and observe gravitational waves. LISA's aims include studying the role of massive black holes in galaxy evolution, testing relativistic gravity, determining the population of ultra-compact

galactic binaries, probing the physics of the early universe, observing supermassive and intermediate black holes mergers and mapping spacetime by observing gravitational captures. The LISA drag-free performance goal is 3×10^{-15} m s^{-2} Hz$^{-1/2}$ at 0.1 mHz. By 2009, the LISA Technology Package (LTP) on board the LISA Pathfinder (LPF) ESA mission, with NASA contributions, aims to demonstrate drag-free performance to a level one order of magnitude lower than the LISA requirement, approximately 3×10^{-14} m s^{-2} Hz$^{-1/2}$ in the frequency bandwidth between 1 mHz and 30 mHz.[4] If LTP is successful, it will achieve the best drag-free performance up to present date.

The Astrodynamical Space Test of Relativity using Optical Devices, ASTROD, is a mission concept[5,6] that consists of a constellation of drag-free spacecraft employing laser interferometric techniques with Earth orbiting satellites, to provide high precision measurements of the relativistic parameters $\{\gamma, \beta\}$; improved determination of the orbits of major asteroids; measurement of solar angular momentum via the Lense-Thirring effect and the detection of low-frequency gravitational waves and solar oscillations. ASTROD aims to improve on the LISA drag-free goal by a factor of between 3 and 10, i.e. (0.3-1) $\times 10^{-15}$ m s^{-2} Hz$^{-1/2}$ at 0.1 mHz.[7,8,9,10,11,12] It is worth noting that a ten-fold acceleration noise improvement with respect to LISA, would allow ASTROD to explore relativistic gravity to an uncertainty level of 1 ppb.[7,8,13,14] A simple version of ASTROD, ASTROD I, has been studied as the first step to ASTROD. ASTROD I concept consists of one spacecraft in a solar orbit, carrying out interferometric ranging and pulse ranging with ground stations.[7,8,9] ASTROD I also aims to measure relativistic and solar system parameters and test fundamental laws of spacetime although with less precision than ASTROD.

Other mission concepts to follow on from LISA are BBO[15] (Big Bang Observer) and DECIGO[16] (DECihertz Interferometry Gravitational wave Observatory). These missions aim to observe the cosmic gravitational wave background produced by standard inflation, having optimum sensitivity around 0.1 Hz, where white dwarf binaries confusion level is thought to be very low. The drag-free force noise requirement for BBO and DECIGO is approximately a hundredth of the LISA force noise target.

In section 2 we report general ideas that ASTROD could adopt to improve drag-free performance, we summarize acceleration and sensor back action disturbances, emphasizing the most significant low-frequency noise sources. Charging disturbances and discharging schemes are briefly discussed in section 3. Finally in section 4 we discuss the performance and problems associated with inertial sensors for other follow on LISA missions. Gravitational interactions are described in terms of multipole moments and a detailed calculation of capacitances for the case of a three dimensional capacitive sensor/actuator are given in appendix A and B, respectively.

2. ASTROD Inertial Sensor

ASTROD will face new challenges in drag-free technology compared with LISA. First, ASTROD aims to improve the LISA drag-free performance target by a factor of between 3 and 10 at 0.1 mHz. On the other hand, ASTROD will extend the gravitational wave observational bandwidth to frequencies below 0.1 mHz, which is the lowest frequency on the LISA observational bandwidth, down to 5×10^{-6} Hz. To achieve these goals, there are key problems that need to be evaluated and their solutions optimized.

The initial design concept proposed for LISA was that laser beams from remote spacecraft would directly illuminate the proof masses. Issues like laser beam pointing, actuation forces to correctly orientate the proof mass with respect to laser beam, and cross coupling of proof mass degrees of freedom, make this scheme less atractive. A new scheme has been recently discussed, in which the laser beam from the remote spacecraft illuminates a fiducial point in the inertial sensor or spacecraft, rather than the proof mass. The inertial sensor provides positioning and attitude reference, and is also used to actuate the proof mass along the other degrees of freedom. The proof mass could be monitored by employing heterodyne laser metrology. This scheme, so-called separate interferometry, has been adopted recently by LISA.[17] However LISA will not fully exploit all its advantages as it may still use two proof masses per spacecraft as references for two different interferometer arms. ASTROD will employ one proof mass, minimizing disturbances and simplifying control.

Replacing capacitive sensing with optical sensing, for drag-free missions following LISA, has also been widely debated. Optical sensing is more sensitive than electrostatic sensing and it requires almost no coupling between the proof mass and surroundings. Towards that direction many efforts to implement optical sensing have been made in the last few years,[18,19,20,21,22] but further laboratory research is needed to develop a space qualified optical sensing scheme. Light pressure could also be used for active control. A more conservative design would combine an optical sensor and capacitive active control.[23] Larger gaps between the proof mass and electrodes could then be used to minimize disturbances.

Ultimately local gravitational gradients are the limiting factor for drag-free performance. In that context the influence of proof mass geometries (spherical, cylindrical, cubic, polyhedral, etc) on sensitivity and its repercussion for the overall inertial sensor design merits further discussion. For monitoring and correcting length changes due to thermal effects and slow relaxations, ASTROD will use an absolute metrology system.[24]

2.1. *Acceleration noise sources*

To discuss the acceleration noise, we consider a simplified control loop model of a spacecraft and a single proof mass. The acceleration noise is given by,[25,26,27]

$$a_n \approx -KX_{nr} + \frac{F_{str}}{m_p} + \left(\frac{F_{ns} + TN_t}{M} \right) \frac{K}{\omega^2 u} \tag{1}$$

Table 1.   Direct acceleration disturbances. The parameters are defined as follows: λ and E denote cosmic ray impact rate and incident energy, P and T are housing pressure and temperature, respectively, A_P the proof mass cross section, ξ_e and ξ_m are the electrostatic and magnetic shielding factors, respectively, δT_{OB} describes optical bench temperature fluctuations and ξ_{TS} the thermal shielding factor between optical bench and the proof mass, δT_{SC} represents spacecraft temperature fluctuations and α thermal expansion coefficient. Finally k_B, σ and G denote the Boltzman, Stefan-Boltzman and Newton Gravitational constants. The rest of parameters are defined in the text.

Environmental disturbances	
Cosmic rays	$f_c = \frac{\sqrt{2mE\lambda}}{m_p}$
Residual gas	$f_{rg} = \frac{\sqrt{2PA_P}}{m_p}(3k_B T m_N)^{1/4}$
Magnetic susceptibility I	$f_{m1} = \frac{2\chi}{\mu_0\rho\xi_m}\delta B_{SC}\nabla B_{SC}$
Magnetic susceptibility II	$f_{m2} = \frac{\sqrt{2}\chi}{\mu_0\rho\xi_m}\nabla B_{SC}\delta B_{ip}$
Permanent magnetic moment	$f_{m3} = \frac{1}{\sqrt{2}m_p\xi_m}M_r\nabla(\delta B)$
Lorentz I	$f_{L1} = \frac{v}{m_p\xi_e}q\delta B_{ip}$
Lorentz II	$f_{L2} = \frac{v}{m_p\xi_e}B_{ip}\delta q$
Radiometer effect	$f_{re} = \frac{A_P P}{2m_p\xi_{TS}}\frac{\delta T_{OB}}{T}$
Outgassing effect	$f_{og} = 10 f_{re}$
Thermal radiation pressure	$f_{tp} = \frac{8\sigma}{3m_p}\frac{A_P}{c}T^3\frac{\delta T_{OB}}{\xi_{TS}}$
Gravity Gradients	$f_{gg} = \frac{2GM}{r^2}\alpha\delta T_{SC}$

where F_{str} are stray forces directly acting on the proof mass of mass m_p, F_{ns} and TN_t are external forces and thruster force noise acting on the outer spacecraft of mass M. X_{nr} is the sensor readout sensitivity, u is the control loop gain and $\omega \equiv 2\pi f$, where f is the frequency. External forces, thruster noise and readout sensitivity contribute to acceleration noise because of the proof mass-spacecraft coupling K. If the proof mass and spacecraft are highly decoupled, then the acceleration noise will be given by stray forces directly acting on the proof mass.

In Table 1 direct acceleration noise sources with the exception of sensor back action disturbances are listed.[26] Environmental disturbances can be divided into different groups depending on their origin. There are disturbances caused by impacts. Cosmic rays which penetrate the spacecraft shielding and residual gas can deposit momentum onto the proof mass. There are disturbances of magnetic origin. Proof mass magnetic susceptibility, χ, and residual permanent moment, M_r, can interact with the residual local and/or the interplanetary magnetic field, B_{SC} and B_{ip}, respectively. There are also disturbances associated with charge. Residual charge accrued on the proof mass can interact with the interplanetary magnetic field via Lorentz force. Finally, there are disturbances associated with thermal fluctuations on the spacecraft. These include the radiometer and outgassing effects, thermal radiation pressure and gravitational gradients caused by thermally induced spacecraft distortions.

Several key factors needed to quantify the total acceleration noise, such as sensor readout noise, back action forces, and stiffness terms, differ for different types of sensor. As an example, optical sensing is nearly stiffness free, providing high readout sensitivity with very low back action forces. On the other hand, with the widely used capacitive sensor, high sensitivity is achieved at the expense of increased acceleration noise and stiffness. Also, because of the fact that close metallic surfaces are needed (3-4 mm gaps in the case of LISA), other noise contributions due to, for example, patch effects and dielectric losses, become significant.

In the best scenario, the proof mass will ultimately be coupled to the space-craft by gravitational gradients. Force gradients of electrostatic origin can be made negligible by implementing large gaps between the proof mass and the surrounding metallic surfaces. An analysis of proof mass geometries and thermal-gravitational modeling of the spacecraft and payload are necessary to account for gravitational disturbances and stiffness terms.

A preliminary quantitative analysis of acceleration noise parameter requirements for ASTROD is given in Refs. 11 and 12.

2.2. *Low-frequency acceleration noise sources*

The LISA observational bandwidth extends from 0.1 mHz to 0.1 Hz. It has been pointed out that gravitational wave observations extended to frequencies below 0.1 mHz, are desirable in the study of certain astrophysical sources like massive black holes (MBH) binaries at high redshift.[28]

The ASTROD free falling proof masses will be separated by distances of 30 to 60 times longer than those of LISA. ASTROD gravitational wave sensitivity curve will therefore be shifted to lower frequencies than the target LISA bandwidth. At low frequencies, spurious forces acting directly on the proof mass are the dominant source of noise. This is the reason why, for a mission like ASTROD, it is particularly important to identify these sources of noise. An extended discussion of low-frequency acceleration noise sources and low-frequency sensitivity curve for gravitational waves for ASTROD is given in Ref. 11.

Thermal, magnetic and electrostatic effects are sources of low-frequency acceleration noise. Thermal noise arises due to radiometer effect; fluctuating outgassing and thermal radiation pressure assymetries; thermal distortion of the spacecraft and residual gas impacts. The magnitude of these effects for a particular mission are dependent on the mission orbit, which dictates the thermal environment. Suppressing thermal disturbances requires thermal diagnostics,[29] stable electronics, passive and, in some cases, active thermal isolation, thermally conductive electrodes (for the case of electrostatic sensing/actuation) and high vacuum. A preliminary evaluation of thermal disturbances for ASTROD shows that the outgassing effect, thermal radiation pressure and thermally induced gravity gradients could be at levels of about $f_{og} \approx 1.1 \times 10^{-17}$ m s^{-2} Hz$^{-1/2}$, $f_{tp} \approx 8 \times 10^{-18}$ m s^{-2} Hz$^{-1/2}$ and $f_{gg} \approx 5.4 \times 10^{-17}$ m s^{-2} Hz$^{-1/2}$, respectively, at 0.1 mHz. A vacuum pressure of the order of

10^{-6} Pa, and a thermal isolation factor, ξ_{TS}, of about 150, were assumed for these estimates. Below 0.1 mHz, solar irradiance fluctuations become the main cause of temperature fluctuations. Solar irradiance fluctuations become more acute when approaching solar rotational period, which is of the order of 25 days.[28] This aspect will be a crucial factor for the thermal diagnostic and thermal isolation system design for ASTROD.

Magnetic noise at low frequencies is caused by interplanetary magnetic field fluctuations, local gradients and magnetic field fluctuations, eddy current damping, magnetic impurities, Lorentz forces due to proof mass residual charge, etc. Suppression of magnetic disturbances requires further reduction and shielding of permanent magnets in the payload, improving magnetic shielding, adopting a magnetic clean wiring (i.e, solar array rewiring, etc) and power system. The most significant magnetic low-frequency noise source is due to the interaction of proof mass magnetic susceptibility with the interplanetary field fluctuations, f_{m2} (see Table 1). Assuming parameter values given in Ref. 11, $f_{m2} \approx 2 \times 10^{-17}$ m s^{-2} Hz$^{-1/2}$ at 0.1 mHz. Disturbance f_{m2} increases at low frequencies as $f^{-2/3}$.

Other relevant noise sources at low frequencies are caused by electrostatic effects, i.e., due to voltage noise, charge fluctuations, DC voltages, dielectric losses, actuation noise, etc. When employing capacitive sensing, the strategies to suppress these noise sources are: increasing the separation between the proof mass and the electrodes, active compensation of DC voltages,[30] avoidance of DC voltages applied to drag-free degrees of freedom, high quality surface coatings to minimize dielectric losses, high stability power supplies and continuous discharging of the proof mass. Electrostatic noise is caused by the capacitive sensor/actuator.

An obvious way for suppression of these noise sources is to replace capacitive sensing by optical sensing. Nevertheless, other concerns will arise if optical sensing is to be used. Thermal distortion of optical components and changes in refractive index with temperature modify optical paths. Because these noise sources are due to thermal fluctuations, they will also be of significance at low frequencies. New ideas addressing these problems, such as using all reflective optics, by using gratings, has been extensively discussed in the literature.[19] Diffractive gratings have also been considered to enhance angular sensitivity, compared with standard angular sensors based on laser reflection.[22]

2.3. *Gravitational modelling*

Drag-free performance will ultimately be limited by local gravitational fields and field gradients. Because of structural distortion of the spacecraft due to thermal fluctuations, thermal and gravitational disturbances need to be modelled together. For the present discussion, we will be concerned only with the local gravitational interaction between the test mass and a simplified spacecraft structure.

We consider three different proof mass geometries: spherical, cylindrical and cuboid. For simplicity, the spacecraft will be assumed to be a hollow cylinder, as a

first approximation.

Following appendix A, we can analyze the gravitational interaction by means of inner, q_{lm}, and outer multipole moments, Q_{lm}, that describe the proof mass, and the spacecraft and payload mass distribution, respectively. Using expression A.3, the first non-zero outer multipole contribution of a hollow cylinder is Q_{20}. Expression A.5 shows that Q_{20} couples to the proof mass inner multipoles q_{00}, $q_{1\pm1}$, q_{20}, $q_{2\pm1}$ and $q_{2\pm2}$.

The first non-zero inner multipole moments for a parallelepiped proof mass of sides 2a, 2b and 2c are $q_{00} = m_p/\sqrt{4\pi}$, $q_{20} = 2/3\sqrt{5/4\pi}m_p\left(2c^2 - a^2 - b^2\right)$ and $q_{2\pm2} = 1/12\sqrt{15/2\pi}m_p(a^2 - b^2)$. On the other hand for a cylindrical proof mass of radius R and semi-height h, we have $q_{00} = m_p/\sqrt{4\pi}$ and $q_{20} = m_p\sqrt{5/4\pi}\left(h^2/3 - R^2/4\right)$. Given these values, it can be seen that the quadrupole moments vanish for a cubic proof mass (as the one adopted by LISA). In the case of ASTROD I, a proof mass of dimensions $50 \times 50 \times 35$ mm is considered. In that case $q_{2\pm2}$ vanishes but not q_{20}. To first order in the gravitational interaction with a cylindrical tube the q_{20} term appears as a constant energy term and will not contribute to the gravitational force. Disturbances proportional to proof mass cross section area can then be minimized by shortening one of the dimensions (as is the case of ASTROD I proof mass). A trade off between the acceleration disturbances which are proportional to proof mass cross sectional area, and the gravitational interaction needs to be done. If a cylindrical proof mass is utilized we can also suppress quadrupole gravitational interaction by choosing $h/R = \sqrt{3}/2$. In the same way disturbances proportional to cross sectional area can be suppressed by shortening h, without altering gravitational interaction with "far away" gravitational asymmetries. A preliminary analysis of gravitational force gradients for ASTROD I is given in Ref. 31.

Another issue that needs to be considered for ASTROD is the fact that the relative distances and angles between the spacecraft are not constant along their orbits. Therefore, telescopes utilized for laser beam pointing need to be steered during the mission. For active gravitational compensation ASTROD will employ dummy telescopes.[7,12]

2.4. *Back action disturbances*

When deciding which type of sensor to use, there are two main options to consider. First, we could consider a low-stiffness sensor. In that case, the proof mass is highly decoupled from the spacecraft, at the expense of losing sensitivity. The other option is to employ a high-stiffness sensor to achieve better readout sensitivity, at the expense of a high level of coupling between the proof mass and the surrounding structure. Capacitive sensing exemplifies this issue. To improve sensitivity we need to place the electrodes closer to the proof mass. By doing that, the stiffness and back action disturbances increase (see Table 2).

To understand the principle behind stiffness and back action disturbances due

to electrostatic sensing and actuation, we first consider the total mechanical energy for a capacitive sensor-proof mass system. Following Refs. 25 and 27, the total mechanical energy is given by

$$W = -\frac{1}{2}\sum_i C_i(V_i - V_s)^2 + \frac{1}{2}\frac{q^2}{C} + qV_s \tag{2}$$

where q is the net charge of the proof mass; C is the coefficient of capacitance of the proof mass: $C = \sum_i C_i$, where $i = x_1, x_2, y_1, y_2, z_1, z_2, g$ defines the capacitances formed by an electrode facing a proof mass side, and capacitance to ground, C_g; V_s is the voltage induced on the proof mass due to the applied voltages, V_i, and voltage to ground, V_g: $V_s = C^{-1}\sum_i C_i V_i$.

The force acting along a generic direction, assuming neither charge and voltage gradients, is given by

$$F = \frac{1}{2}\sum_i C_i'(V_i - V_M)^2 \tag{3}$$

where $V_M = V_s + \frac{q}{C}$, and C_i' is the derivative of capacitance C_i along the generic direction.

Force disturbances can then be considered of two types: a) position dependent disturbances, caused by fluctuating position and attitude of the proof mass (stiffness terms), and b) position independent disturbances, caused by voltage and charge fluctuations. Along a generic sensitive (drag-free) axis, we can write the fluctuating force terms due to charge and voltage fluctuations as

$$\delta F_{\delta V,1} = \left(\sum_i C_i'(V_i - V_s) - V_{m_1}'C\right)\delta V_i \tag{4}$$

$$\delta F_{\delta V,2} = \left(\sum_i C_i'\frac{q}{C} + V_{m_2}'\sum_i C_i\right)\delta V_i \tag{5}$$

$$\delta F_{\delta q,1} = V_{m_1}'\delta q \tag{6}$$

$$\delta F_{\delta q,2} = V_{m_2}'\delta q \tag{7}$$

where

$$V_{m_1}' = \frac{1}{C}\sum_i C_i'(V_i - V_s) \tag{8}$$

and

$$V_{m_2}' = -\frac{q}{C^2}\sum_i C_i' \tag{9}$$

Table 2 shows the back action disturbances given above for the special case of a one dimensional capacitive sensor and one translational degree of freedom.[26] Disturbances due to dielectric losses and patch fields are also listed. An extended

Table 2. Sensor back action acceleration disturbances. The parameters are defined as follows: δv_{diel} denotes voltage fluctuation due to dielectric losses, V_0 is dc bias voltage, V_{pe} average patch potential, V_{x0} average potential across opposite side of sensor, δV_d fluctuations in voltage different across opposite side of sensor and d is the gap between the proof mass and surrounding housing and electrodes. The rest of parameters are defined in the text.

Back action disturbances	
Dielectric losses	$f_{DL} = \frac{\sqrt{2}C_x}{m_p d} V_0 \delta v_{diel}$
Patch fields (Uncompensated)	$f_{pe} = \frac{1}{m_p d} \frac{C_x}{C} V_{pe} \delta q$
$\delta V_d \times V_{0g}$	$f_{\delta V,1} = \frac{C_x}{m_p d} \frac{C_x}{C} (V_{x0} - V_g) \delta V_d$
$\delta V_d \times q$	$f_{\delta V,2} = \frac{q}{m_p d} \frac{C_x}{C} \delta V_d$
$\delta q \times V_d$	$f_{\delta q,1} = \frac{1}{m_p d} \frac{C_x}{C} V_d \delta q$
$\delta q \times q$	$f_{\delta q,2} = \frac{q}{m_p d^2} \frac{C_x}{C^2} \Delta d \delta q$

discussion of electrostatic back action disturbances for ASTROD I and ASTROD can be found in Ref. 27 and 11, respectively.

Position dependent disturbances (stiffness terms) can be obtained by calculating the variations in capacitances, δC_i, and capacitance gradients, $\delta C_i'$.

In appendix B formulae for capacitances, capacitance gradients and their fluctuations, given by C_i, C_i', δC_i and $\delta C_i'$, respectively, are obtained for the special case of a 6-degree of freedom, cubic, capacitive sensor. These expressions codify cross-coupling effects between translational and rotational degrees of freedom.

On the other hand, optical sensing offers advantages in terms of high sensitivity and low back action forces. Optical readout sensitivity is ultimately limited by laser shot noise. Laser shot noise is proportional to $P^{-1/2}$, where P is the laser power. Lasing back action force is proportional to the laser power, and is given by $2P/c$, where c is the speed of light. This force can, in principle, be compensated to a high degree of accuracy.

3. Charging disturbances

Galactic cosmic rays (GCR) and solar energetic particles (SEP) incident on the spacecraft will result in the accumulation of charge on the proof mass. Charge accrued on the proof mass leads to numerous sources of noise. Some of these noise sources have been described and discussed above. First, when summarizing direct acceleration noise sources, the Lorentz force due to the movement of the charged proof mass through the interplanetary magnetic field was discussed. We have also discussed, in the particular case of employing capacitive sensing/actuation, how the proof mass charge couples to sensing/actuation voltages to induce spurious forces and stiffness terms that will affect the performance of the inertial sensor.

Disturbances associated with charging can be divided into three types: a) those which are proportional to charge accrued, q, b) those proportional to δq, which are so-called "shot noise" terms and c) mixed terms proportional to $q\delta q$. This division

is of importance in understanding disturbance suppression schemes (see discussion below).

Time dependent forces also contribute to the spectral noise density. Proof mass charging is a time dependent process and both Coulomb and Lorentz forces give rise to coherent Fourier signals (CHS). Assuming a linear increase of proof mass charge with time, the total charge can be written as $q(t) = \bar{\dot{q}}t + \delta q$, where $\bar{\dot{q}}$ is the mean charging rate. Following Ref. 32 the acceleration noise terms due to Coulomb and Lorentz interactions are given by

$$a_{CHS} = h_k(t) = (\phi_k + \Theta_k)\, t + \Xi_k t^2 \qquad (10)$$

where

$$\phi_k = \frac{\bar{\dot{q}}vB_{ip}}{m_p\xi_e}, \;\; \Theta_k = \frac{\bar{\dot{q}}C_x}{m_pCd}V_d, \text{ and } \Xi_k = \frac{2C_x}{m_p}\left(\frac{\bar{\dot{q}}}{Cd}\right)^2\Delta d \qquad (11)$$

using a parallel plate approximation to estimate capacitances and capacitance derivatives. The parameters used above are defined as follows: v is the orbital velocity of the proof mass, B_{ip} is the interplanetary magnetic field, ξ_e is the electrostatic shielding factor, C_x is the capacitance along the sensitive axis, V_d is the voltage difference between opposite sensor sides, and d and Δd are the capacitance gap and gap asymmetry, respectively.

Inspection of (11) shows that geometrical and electrostatic asymmetries in the inertial sensor contribute to the appearance of these signals. Geometrical asymmetry arises due to limited machining accuracy and it is represented by an asymmetry in the capacitance gap. Electrostatic asymmetry is due to a stray DC potential imbalance between opposite sides of the sensor. These residual DC stray potentials are dependent on the work function of the metallic surfaces. These potentials are measurable in average, for each electrode, and can be balanced by appropriate applied bias voltages.[30] Ultimately, voltage offset compensation will depend on voltage measurement precision required and work function domains stability in periods of time comparable with the measurement integration time. In the context of LISA mission, these coherent Fourier signals can exceed the instrumental noise target, for typical parameter values.[32]

At low frequencies, charging disturbances and coherent charging signals are of particular concern. Those so-called "shot noise" charging disturbances and coherent signals scale, roughly speaking, with frequency as $1/f$.[32] Of special note is the acceleration disturbance proportional to residual voltage difference across opposite sides of the sensor and charge fluctuations, $f_{\delta q,1}$ (see Table 2). By active compensation, the potential difference across opposite sensor sides can be balanced to ~ 1 mV.[30] To improve on the LISA acceleration noise by a factor of 10 at 0.1 mHz, ASTROD would need to reduce this value to below 0.7 mV,[12] giving a disturbance level $f_{\delta q,1} \approx 1.4 \times 10^{-16}$ m s^{-2} Hz$^{-1/2}$.

3.1. *Discharging schemes*

When discussing discharging schemes we have to keep in mind that not only charge accrued by the proof mass but also the charging rate are potential causes of noise.[33,34] Discharging the proof mass will suppress some charging disturbances and will reduce the coupling of the proof mass with its surroundings. Coherent signals are proportional to mean charging rate. By "mean charging rate" we mean that charging and discharging rates are added linearly to give a net rate. Therefore by accurately matching charging and discharging rates, these signals can be suppressed.[32] Nevertheless the fact that proof mass discharging involves the transport of charge "packages", will cause additional shot noise. Shot noise due to proof mass charging and discharging cannot partially cancel each other because the charging and discharging processes are statistically independent. Therefore their respective shot noise terms have to be added quadratically.

For LISA, a continuous discharging scheme will be adopted. The continuous discharging process will consist basically of two steps. Firstly, the proof mass charge needs to be accurately measured. That can be done by applying a sinusoidal dither voltage and measuring the displacement along a non drag-free axis. This proof mass displacement is proportional to proof mass charge. Secondly, UV light will shine on the proof mass and/or surrounding electrodes to discharge the proof mass via the photoelectric effect.[32,33,34]

The ASTROD strategy to suppress charging noise will depend on which sensing/actuation device is employed. ASTROD could benefit from the replacement of capacitive sensing by optical sensing. Even if a capacitive scheme is employed for force actuation, charging disturbances and coherent signals could be suppressed by increasing the gaps between the test mass and surrounding surfaces. If optical force actuation is employed, then only Lorentz type disturbances need to be considered. In that case, the charging requirements can be relaxed and the discharging scheme can be simplified.

4. Inertial sensors for other missions to test fundamental physics

Follow on LISA mission concepts have been proposed, not only to extend the observational bandwidth to lower frequencies, but also to fill the gap between space antennae and ground based interferometric facilities (LIGO, GEO600, VIRGO, Advanced LIGO, LCGT, etc). Follow-on mission concepts include the Big Bang Observer (BBO) and the Japanese antenna DECi-hertz Interferometer Gravitational wave Observer (DECIGO). Both BBO and DECIGO are to be designed to have an optimum sensitivity between 0.1 Hz and 10 Hz. The objectives of the decihertz antennae are: measuring the expansion rate of the universe; determining the equation of state of dark energy, by observing the coalescence of binary neutron stars and stellar mass black holes; and shedding light on the growth of supermassive black holes, by studying the merger of intermediate mass black holes.[15,16]

These missions will also measure the relative distance, or maintain the distance

by feedback, between test masses in nearly free fall. To achieve their objectives they need to reduce residual spurious forces to approximately a hundredth of the LISA goal.

These missions are conceptually different. To shift the gravitational wave sensitivity curve towards the decihertz level, the effective interferometer arm length has to be, approximately, a hundredth of the LISA arm length (5×10^6 km). The BBO preliminary conceptual design consists of a constellation of spacecraft with a LISA-type design and an arm length of 5×10^4 km. On the other hand, DE-CIGO plans to place in space a Fabry-Perot cavity of length 1000 km and finesse of approximately 10. To accomplish this, DECIGO would place massive mirrors of 100 kg mass and 1 meter diameter in free fall. Large actuation forces, to keep the cavity in resonance, will be required. This condition and the stringent residual acceleration noise levels, of the order of 4×10^{-19} m s^{-2} Hz$^{-1/2}$, seem to be difficult to reconcile. Nevertheless one could employ a large control loop gain to minimize the acceleration disturbances due to actuation forces. Other technological difficulties common to both missions are related to the requirement for low residual gas pressure. Extremely low pressure could be achieved by venting some of the gas to outer space. However, this could cause other problems such as drag of the proof mass because of residual gas flow, and undesired particles coming from the thruster propellant, brought into the proof mass housing.

Acknowledgments

References

1. B. Lange, The Drag-free Satellite, *AIAA Journal* **2(9)**, 1950 (1964); B. Lange, The Control and Use of Drag-free Satellites, Ph.D SUDAER 194, June 1964. http://www.dragfreesatellite.com.
2. Gravity Probe B. http://einstein.stanford.edu.
3. LISA, Laser Interferometer Space Antenna: A Cornerstone Mission for the Observation of Gravitational Waves, ESA System and Technology Study Report, ESA-SCI 11, 2000.
4. S. Anza et al. *Class. Quantum Grav.* **22** S125 (2005).
5. A. Bec-Borsenberger, J. Christensen-Dalsgaard, M. Cruise, A. Di Virgilio, D. Gough, M. Keiser, A. Kosovichev, C. Lmmerzahl, J. Luo, W.-T. Ni, A. Peters, E. Samain, P. H. Scherrer, J.-T. Shy, P. Touboul, K. Tsubono, A.-M. Wu and H.-C. Yeh, Astrodynamical Space Test of Relativity using Optical Devices ASTROD — A Proposal Submitted to ESA in Response to Call for Mission Proposals for Two Flexi-Missions F2/F3, January 31, 2000; and references there in.
6. W.-T. Ni, *Int J. Mod. Phys D* **11(7)**, 947 (2002) ; and references therein.
7. W.-T. Ni, ASTROD and ASTROD I: an overview, to appear in *Gen. Rel. Grav.* **39** (2007).

8. W.-T. Ni, ASTROD and ASTROD I, to appear in *Nuclear Physics B (Proceedings Supplements). Spacepart 06 Conf. Proc.*-in press (2007).
9. W.-T. Ni, ASTROD and ASTROD I: overview and progress, *Int. J. Mod. Phys. D*, xxx, this issue (2007).
10. W.-T. Ni, S. Shiomi and A.-C. Liao, *Class. Quantum Grav.* **22** S269 (2005).
11. A. Pulido Patón and W.-T. Ni, The low-frequency sensitivity to gravitational waves for ASTROD, to appear in *Gen. Rel. Grav.* **39** (2007).
12. A. Pulido Patón, ASTROD Gravitational Reference Sensor (GRS): goal and requirements, to appear in *Nuclear Physics B (Proceedings Supplements). Spacepart 06 Conf. Proc.* Reference: NUPHBP 11611-in press (2007).
13. Wei-Tou Ni, Antonio Pulido Patón and Yan Xia. Testing Relativistic Gravity to One Part per Billion, in Lasers, Clocks, and Drag-Free: Exploration of Relativistic Gravity in Space, Eds. Hansjrg Dittus, Claus Lmmerzahl and Slava G. Turyshev. Springer (2007).
14. W.-T. Ni, *Int. J. Mod. Phys. D*, **14**(6), 901 (2005).
15. J. Crowder and N.J. Cornish. *Phys. Rev. D* **72**, 083005 (2005); and references therein.
16. S. Kawamura, et al. *Class. Quantum Grav.* **23** S125 (2006).
17. G. Heinzel et al. *Class. Quantum Grav.* **23** S119 (2006).
18. F. Acernese et al. *Class. Quantum Grav.* **22** S279 (2005).
19. Ke-Xun Sun et al., *Class. Quantum Grav.* **22** S287 (2005).
20. C.C. Speake and S.M. Aston, *Class. Quantum Grav.* **22**, S269 (2005).
21. X. Xu and W-T. Ni, *Adv. Space Res.* **32 (7)**, 1443 (2003).
22. Ke-Xun Sun, Saps Buchman and Robert Byer, *Journal of Physics: Conference Series* **32**, 167, (2006).
23. Clive Speake and Stuart Aston, in Gravitational Wave and Particle Astrophysics Detectors, Eds. James Hough, Gary H. Sanders, *Proc. of SPIE* **5500**, 120 (2004).
24. W.-T. Ni et al, *Adv. Space Res.* **32**, 1437 (2003).
25. S. Vitale et al., *Nucl. Phys. B (Proc. Suppl.)* **110**, 209 (2002).
26. B. L. Schumaker, *Class. Quantum Grav.* **20**, S239 (2003).
27. S. Shiomi and W.-T. Ni, *Class. Quantum Grav.* **23**, 4415 (2006).
28. P. L. Bender, *Class. Quantum Grav.* **20**, S301 (2003).
29. A. Lobo et al. *Class. Quantum Grav.* **23** 5177 (2006).
30. W. J. Weber et al, arXiv : gr-qc / 0309067 v1 (13 Sept 2003).
31. Sachie Shiomi, *Journal of Physics: Conference Series* **32**, 186, (2006).
32. D. N. A. Shaul et al, *Int. J. Mod. Phys. D* **14**, 51 (2005).
33. D. N. A. Shaul et al, Charge management for LISA and LISA Pathfinder, *Int. J. Mod. Phys. D*, xxx, this issue, (2007).
34. Ke-Xun Sun et al. *Class. Quantum Grav.* **23** S141 (2006).
35. J. D. Jackson, *Classical Electrodynamics*, 3rd edn. (John Wiley and Sons, Inc, 1998), p. 145.
36. Christian D'Urso and E. G. Adelberger, *Phys. Rev. D* **55** (12), 7970 (1997).

Appendix A.   Gravitational interaction in terms of multipole moments

The gravitational potential can be written in terms of multipole moments as[31,35]

$$V = -4\pi G \sum_{l=0}^{\infty} \sum_{m=-l}^{l} \frac{1}{2l+1} q_{lm} Q_{lm} \tag{A.1}$$

where q_{lm} (Q_{lm}) are the inner (outer) moments defined respectively by

$$q_{lm} = \int_{v_t} \rho_t(\vec{x}')r'^l Y_{lm}^*(\theta', \phi')d^3\vec{x}' \tag{A.2}$$

and

$$Q_{lm} = \int_{v_s} \rho_s(\vec{x})r^{-(l+l)}Y_{lm}(\theta, \phi)d^3\vec{x} \tag{A.3}$$

If the inner multipoles of the test mass, q_{lm}, are known in a given reference frame, then the inner multipoles with respect to a new reference frame, can be obtained. Let us consider a position $\vec{r}'' = \vec{r}' + \vec{r}$. The test mass position with respect to the reference frame, of origin O, in which the multipoles are known are denoted by $\vec{r}$. On the other hand, $\vec{r}'$ denotes the position vector of the origin O, with respect to the new reference frame in which we wish to work out the multipoles. In the special case of pure translations,[36]

$$r''^L Y_{LM}^*(\theta, \phi) = \sum_{l,l'=0}^{L} \sum_{m,m'} \sqrt{\frac{4\pi(2L+1)!}{(2l'+1)!(2l+1)!}} r'^{l'} r^l \times$$
$$\delta_{L,l+l'} C(l', m', l, m, L, M) Y_{l'm'}^*(\theta', \phi') Y_{lm}(\theta, \phi) \tag{A.4}$$

Using eq. A.4 we can rewrite the gravitational potential energy A.1 in terms of the known inner multipoles and the translational parameters between the two reference frames as

$$V(\vec{r}) = -4\pi G \sum_{L=0}^{\infty} \sum_{M=-L}^{L} \frac{1}{2L+1} Q_{LM} \times$$
$$\sum_{l,l'=0}^{L} \sum_{m,m'} \sqrt{\frac{4\pi(2L+1)!}{(2l'+1)!(2l+1)!}} C(l', m', l, m, L, M) \delta_{L,l+l'} r^{l'} Y_{l'm'}^*(\theta, \phi) q_{lm} \tag{A.5}$$

The gravitational force can be then easily calculated by taking the derivatives of A.5 with respect to the translational parameters.

Appendix B. A cubical inertial sensor. Capacitance calculations

We consider a six-dimensional degree of freedom model for the capacitive sensing/actuation device. A cuboid proof mass of side lengths $(2L_x, 2L_y, 2L_z)$ is inserted into a three dimensional capacitive sensor. The gaps at the equilibrium position between the proof mass and the electrodes are denoted by (D_x, D_y, D_z). The proof mass translational degrees of freedom are denoted by (d_x, d_y, d_z). The proof mass rotational degrees of freedom are given by the Euler angles (ϕ, θ, ψ), in the so-called "x-convention".

We first consider the electrostatic energy density to work out capacitances for this model. If the electric field between two conducting surfaces is defined by $\vec{E}$, then

the electrostatic energy density is given by $\omega = \frac{1}{2}\varepsilon_0 E^2$. The proof mass faces and the electrodes will define the capacitances. In the case in which the displacement and rotation of the proof mass are infinitesimal, we can approximate the electric field between conducting surfaces by $\vec{E}_i \simeq \frac{(V_M - V_i)}{\triangle x_i}\vec{u}_i$, where V_M (V_i) and $\triangle x_i$ denote the proof mass (electrode) potential and the capacitance gap in the i-direction, respectively. The electrostatic energy is then given by

$$W^{\pm}(d_x, d_y, d_z, \phi, \theta, \psi) \simeq \frac{1}{2}\varepsilon_0(V_M - V_i)^2 \int \frac{dV}{\triangle x_i^{\pm 2}} \tag{B.1}$$

where by the simbol $\pm$ we differentiate between the gaps at opposite sides of the sensor.

By integrating along the gap (in this case we choose the gap along the z-axis), the electrostatic energy can be written as

$$W^{\pm}(d_x, d_y, d_z, \phi, \theta, \psi) \simeq -\frac{1}{2}\varepsilon_0(V_M - V_i)^2 \int \frac{dxdy}{\triangle x_i^{\pm}(x, y, d_x, d_y, d_z, \phi, \theta, \psi)} \tag{B.2}$$

and we can define the capacitances by

$$C_{x_i}^{\pm}(d_x, d_y, d_z, \phi, \theta, \psi) \simeq \varepsilon_0 \int dx_j dx_k \frac{1}{\triangle x_i^{\pm}(x_j, x_k, d_x, d_y, d_z, \phi, \theta, \psi)} \tag{B.3}$$

The information about how different degrees of freedom couple to each other is codified in B.3.

To explicitly work out capacitances, we translate and rotate the proof mass by the parameters $(d_x, d_y, d_z, \phi, \theta, \psi)$.

The rotation matrix in terms of the Euler angles (ϕ, θ, ψ) is written as

$$N(\phi, \theta, \psi) =$$

$$\begin{pmatrix} \cos\psi\cos\phi - \cos\theta\sin\phi\sin\psi & \cos\psi\sin\phi + \cos\theta\cos\phi\sin\psi & \sin\psi\sin\theta \\ -\sin\psi\cos\phi - \cos\theta\sin\phi\cos\psi & -\sin\psi\sin\phi + \cos\theta\cos\phi\cos\psi & \cos\psi\sin\theta \\ \sin\theta\sin\phi & -\sin\theta\cos\phi & \cos\theta \end{pmatrix} \tag{B.4}$$

Given this matrix we can define the normal vectors to the proof mass faces after a (ϕ, θ, ψ)-rotation, with respect to a fixed reference frame. This reference frame has its origin in the geometrical center of the sensor and its axis orthogonal to electrode surfaces. The normal vectors can be written as

$$n_1 = \begin{pmatrix} n_{1x} \\ n_{1y} \\ n_{1z} \end{pmatrix} = \begin{pmatrix} \cos\psi\cos\phi - \cos\theta\sin\phi\sin\psi \\ \cos\psi\sin\phi + \cos\theta\cos\phi\sin\psi \\ \sin\psi\sin\theta \end{pmatrix} \tag{B.5}$$

$$n_2 = \begin{pmatrix} n_{2x} \\ n_{2y} \\ n_{2z} \end{pmatrix} = \begin{pmatrix} -\sin\psi\cos\phi - \cos\theta\sin\phi\cos\psi \\ -\sin\psi\sin\phi + \cos\theta\cos\phi\cos\psi \\ \cos\psi\sin\theta \end{pmatrix} \tag{B.6}$$

$$n_3 = \begin{pmatrix} n_{3x} \\ n_{3y} \\ n_{3z} \end{pmatrix} = \begin{pmatrix} \sin\theta\sin\phi \\ -\sin\theta\cos\phi \\ \cos\theta \end{pmatrix} \tag{B.7}$$

The equations of the proof mass faces, are defined by

$$\left(\vec{x} - \vec{P_i}\right) \cdot \vec{n}_i = 0 \tag{B.8}$$

where $\vec{P_i} = \pm L_i n_i + \vec{d}$, being $\vec{d} \equiv (d_x, d_y, d_z)$ a displacement, and L_i defines the semi-length of the proof mass along the three axes x, y and z.

Using this expressions we can obtain the capacitance gaps for the three directions. These are given by

$$\triangle x^{\pm} = F_x^{\pm} \pm \left(y + A_x^{\pm}\right) n_1^x \pm \left(z + B_x^{\pm}\right) n_2^x \tag{B.9}$$

$$\triangle y^{\pm} = F_y^{\pm} \pm \left(x + A_y^{\pm}\right) n_1^y \pm \left(z + B_y^{\pm}\right) n_2^y \tag{B.10}$$

$$\triangle z^{\pm} = F_z^{\pm} \pm \left(x + A_z^{\pm}\right) n_1^z \pm \left(y + B_z^{\pm}\right) n_2^z \tag{B.11}$$

We define the capacitances as

$$C_{x,up}^{\pm} = \varepsilon_0 \int_0^{L_y} dy \int_{-L_z}^{L_z} dz \frac{1}{\triangle x^{\pm}(y,z)} \tag{B.12}$$

$$C_{x,down}^{\pm} = \varepsilon_0 \int_{-L_y}^{0} dy \int_{-L_z}^{L_z} dz \frac{1}{\triangle x^{\pm}(y,z)} \tag{B.13}$$

$$C_{y,up}^{\pm} = \varepsilon_0 \int_{-L_x}^{L_x} dx \int_0^{L_z} dz \frac{1}{\triangle y^{\pm}(y,z)} \tag{B.14}$$

$$C_{y,down}^{\pm} = \varepsilon_0 \int_{-L_x}^{L_x} dx \int_{-L_z}^{0} dz \frac{1}{\triangle y^{\pm}(y,z)} \tag{B.15}$$

$$C_{z,left}^{\pm} = \varepsilon_0 \int_0^{L_x} dx \int_{-L_y}^{L_y} dy \frac{1}{\triangle z^{\pm}(x,y)} \tag{B.16}$$

$$C_{z,right}^{\pm} = \varepsilon_0 \int_{-L_x}^{0} dx \int_{-L_y}^{L_y} dy \frac{1}{\triangle z^{\pm}(x,y)} \tag{B.17}$$

where by up, down, left, right, we indicate that two electrodes face each proof mass face (see Fig. 1).

The capacitances in the x-direction are given by

$$C_{x,up}^{+} = \frac{\varepsilon_0}{n_2} L_y \ln \frac{F_x^+ + (L_z + B_x^+)n_2^x + (A_x^+ + L_y)n_1^x}{F_x^+ + (B_x^+ - L_z)n_2^x + (A_x^+ + L_y)n_1^x}$$
$$- \frac{\varepsilon_0}{n_2^x} \frac{F_x^+ + (L_z + B_x^+)n_2^x + A_x^+ n_1^x}{n_1^x} \ln \frac{F_x^+ + (L_z + B_x^+)n_2^x + (A_x^+ + L_y)n_1^x}{F_x^+ + (L_z + B_x^+)n_2^x + A_x^+ n_1^x}$$
$$+ \frac{\varepsilon_0}{n_2^x} \frac{F_x^+ + (B_x^+ - L_z)n_2^x + A_x^+ n_1^x}{n_1^x} \ln \frac{F_x^+ + (B_x^+ - L_z)n_2^x + (A_x^+ + L_y)n_1^x}{F_x^+ + (B_x^+ - L_z)n_2^x + A_x^+ n_1^x} \tag{B.18}$$
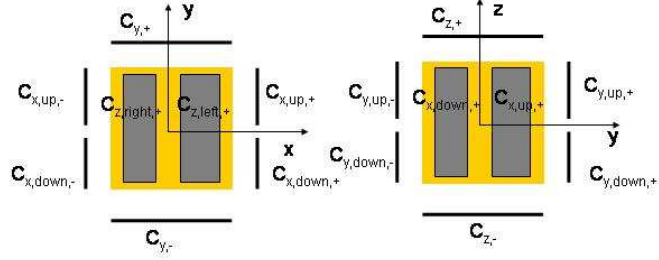
Fig. 1.   Schematic view of capacitive sensing electrodes.

$$C_{x,up}^- = -\frac{\varepsilon_0}{n_2^x} L_y \ln \frac{F_x^- - (L_z + B_x^-)n_2^x - (A_x^- + L_y)n_1^x}{F_x^- - (B_x^- - L_z)n_2^x - (A_x^- + L_y)n_1^x}$$

$$-\frac{\varepsilon_0}{n_2^x} \frac{F_x^- - (L_z + B_x^-)n_2^x - A_x^- n_1^x}{n_1^x} \ln \frac{F_x^- - (L_z + B_x^-)n_2^x - (A_x^- + L_y)n_1^x}{F_x^- - (L_z + B_x^-)n_2^x - A_x^- n_1^x}$$

$$+\frac{\varepsilon_0}{n_2^x} \frac{F_x^- - (B_x^- - L_z)n_2^x - A_x^- n_1^x}{n_1^x} \ln \frac{F_x^- - (B_x^- - L_z)n_2^x - (A_x^- + L_y)n_1^x}{F_x^- - (B_x^- - L_z)n_2^x - A_x^- n_1^x} \tag{B.19}$$

$$C_{x,down}^+ = \frac{\varepsilon_0}{n_2^x} L_y \ln \frac{F_x^+ + (L_z + B_x^+)n_2^x + (A_x^+ - L_y)n_1^x}{F_x^+ + (B_x^+ - L_z)n_2^x + (A_x^+ - L_y)n_1^x}$$

$$+\frac{\varepsilon_0}{n_2^x} \frac{F_x^+ + (L_z + B_x^+)n_2^x + A_x^+ n_1^x}{n_1^x} \ln \frac{F_x^+ + (L_z + B_x^+)n_2^x + (A_x^+ - L_y)n_1^x}{F_x^+ + (L_z + B_x^+)n_2^x + A_x^+ n_1^x}$$

$$-\frac{\varepsilon_0}{n_2^x} \frac{F_x^+ + (B_x^+ - L_z)n_2^x + A_x^+ n_1^x}{n_1^x} \ln \frac{F_x^+ + (B_x^+ - L_z)n_2^x + (A_x^+ - L_y)n_1^x}{F_x^+ + (B_x^+ - L_z)n_2^x + A_x^+ n_1^x} \tag{B.20}$$

$$C_{x,down}^- = -\frac{\varepsilon_0}{n_2^x} L_y \ln \frac{F_x^- - (L_z + B_x^-)n_2^x - (A_x^- - L_y)n_1^x}{F_x^- - (B_x^- - L_z)n_2^x - (A_x^- - L_y)n_1^x}$$

$$+\frac{\varepsilon_0}{n_2^x} \frac{F_x^- - (L_z + B_x^-)n_2^x - A_x^- n_1^x}{n_1^x} \ln \frac{F_x^- - (L_z + B_x^-)n_2^x - (A_x^- - L_y)n_1^x}{F_x^- - (L_z + B_x^-)n_2^x - A_x^- n_1^x}$$

$$-\frac{\varepsilon_0}{n_2^x} \frac{F_x^- - (B_x^- - L_z)n_2^x - A_x^- n_1^x}{n_1^x} \ln \frac{F_x^- - (B_x^- - L_z)n_2^x - (A_x^- - L_y)n_1^x}{F_x^- - (B_x^- - L_z)n_2^x - A_x^- n_1^x} \tag{B.21}$$

where

$$F_x^{\pm} \equiv L_x(1 - n_{1x}) + D_x \mp d_x \tag{B.22}$$

$$A_x^{\pm} \equiv \mp L_x n_{1y} - d_y \tag{B.23}$$

$$B_x^{\pm} \equiv \mp L_x n_{1z} - d_z \tag{B.24}$$

$$n_1^x \equiv \frac{n_{1y}}{n_{1x}} \tag{B.25}$$

$$n_2^x \equiv \frac{n_{1z}}{n_{1x}} \tag{B.26}$$

The capacitances in the y-direction are

$$C_{y,up}^{\pm} = C_{x,up}^{\pm}((L_y, L_z, A_x^{\pm}, B_x^{\pm}, n_1^x, n_2^x) \to (L_z, L_x, B_y^{\pm}, A_y^{\pm}, n_2^y, n_1^y)) \tag{B.27}$$

$$C_{y,down}^{\pm} = C_{x,down}^{\pm}((L_y, L_z, A_x^{\pm}, B_x^{\pm}, n_1^x, n_2^x) \to (L_z, L_x, B_y^{\pm}, A_y^{\pm}, n_2^y, n_1^y)) \tag{B.28}$$

where

$$F_y^{\pm} \equiv L_y(1 - n_{2y}) + D_y \mp d_y \tag{B.29}$$

$$A_y^{\pm} \equiv \mp L_y n_{2x} - d_x \tag{B.30}$$

$$B_y^{\pm} \equiv \mp L_y n_{2z} - d_z \tag{B.31}$$

$$n_1^y \equiv \frac{n_{2x}}{n_{2y}} \tag{B.32}$$

$$n_2^y \equiv \frac{n_{2z}}{n_{2y}} \tag{B.33}$$

The capacitances in the z-direction are given by

$$C_{z,left}^{\pm} = C_{x,up}^{\pm}(L_z \to L_y; L_y \to L_x) \tag{B.34}$$

$$C_{z,right}^{\pm} = C_{x,down}^{\pm}(L_z \to L_y; L_y \to L_x) \tag{B.35}$$

where now

$$F_z^{\pm} \equiv L_z(1 - n_{3z}) + D_z \mp d_z \tag{B.36}$$

$$A_z^{\pm} \equiv \mp L_z n_{3x} - d_x \tag{B.37}$$

$$B_z^{\pm} \equiv \mp L_z n_{3y} - d_y \tag{B.38}$$

$$n_1^z \equiv \frac{n_{3x}}{n_{3z}} \tag{B.39}$$

$$n_2^z \equiv \frac{n_{3y}}{n_{3z}} \tag{B.40}$$

We can approximate the expressions of capacitances by taking into account that $F \gg A$ and B. Then we have

$$C_{x,up}^{+} = 2\varepsilon_0 L_y L_z \frac{1}{F_x^{+} + B_x^{+} n_2^x + (A_x^{+} + L_y)n_1^x} \tag{B.41}$$

$$C_{x,up}^{-} = 2\varepsilon_0 L_y L_z \frac{1}{F_x^{-} - B_x^{-} n_2^x - (A_x^{-} + L_y) n_1^x} \tag{B.42}$$

$$C_{x,down}^{+} = 2\varepsilon_0 L_y L_z \frac{1}{F_x^{+} + B_x^{+} n_2^x + (A_x^{+} - L_y) n_1^x} \tag{B.43}$$

$$C_{x,down}^{-} = 2\varepsilon_0 L_y L_z \frac{1}{F_x^{-} - B_x^{-} n_2^x - (A_x^{-} - L_y) n_1^x} \tag{B.44}$$

To work out the force and the force disturbance along the sensitive axis we also need to work out capacitance gradients, which are given by

$$\frac{\partial C_{x,up}^{+}}{\partial d_x} = \frac{2\varepsilon_0 L_y L_z}{\left[F_x^{+} + B_x^{+} n_2^x + (A_x^{+} + L_y) n_1^x \right]^2} \tag{B.45}$$

$$\frac{\partial C_{x,up}^{-}}{\partial d_x} = -\frac{2\varepsilon_0 L_y L_z}{\left[F_x^{-} - B_x^{-} n_2^x - (A_x^{-} + L_y) n_1^x \right]^2} \tag{B.46}$$

$$\frac{\partial C_{x,down}^{+}}{\partial d_x} = \frac{2\varepsilon_0 L_y L_z}{\left[F_x^{+} + B_x^{+} n_2^x + (A_x^{+} - L_y) n_1^x \right]^2} \tag{B.47}$$

$$\frac{\partial C_{x,down}^{-}}{\partial d_x} = -\frac{2\varepsilon_0 L_y L_z}{\left[F_x^{-} - B_x^{-} n_2^x - (A_x^{-} - L_y) n_1^x \right]^2} \tag{B.48}$$

Along the y-axis we have

$$\frac{\partial C_{y,up}^{+}}{\partial d_x} = -\frac{2\varepsilon_0 L_x L_z (\phi + \psi)}{\left[F_y^{+} + A_y^{+} n_1^y + (B_y^{+} + L_z) n_2^y \right]^2} \tag{B.49}$$

$$\frac{\partial C_{y,up}^{-}}{\partial d_x} = \frac{2\varepsilon_0 L_x L_z (\phi + \psi)}{\left[F_y^{-} - A_y^{-} n_1^y - (B_y^{-} + L_z) n_2^y \right]^2} \tag{B.50}$$

$$\frac{\partial C_{y,down}^{+}}{\partial d_x} = -\frac{2\varepsilon_0 L_x L_z (\phi + \psi)}{\left[F_y^{+} + A_y^{+} n_1^y + (B_y^{+} - L_z) n_2^y \right]^2} \tag{B.51}$$

$$\frac{\partial C_{y,down}^{-}}{\partial d_x} = \frac{2\varepsilon_0 L_x L_z (\phi + \psi)}{\left[F_y^{-} - A_y^{-} n_1^y - (B_y^{-} - L_z) n_2^y \right]^2} \tag{B.52}$$

Along the z-axis,

$$\frac{\partial C_{z,left}^{+}}{\partial d_x} = \frac{2\varepsilon_0 L_x L_y \phi \theta}{\left[F_z^{+} + B_z^{+} n_2^z + (A_z^{+} + L_x) n_1^z \right]^2} \tag{B.53}$$

$$\frac{\partial C_{z,left}^{-}}{\partial d_x} = -\frac{2\varepsilon_0 L_x L_y \phi \theta}{\left[F_z^{-} - B_z^{-} n_2^z - (A_z^{-} + L_x) n_1^z \right]^2} \tag{B.54}$$

$$\frac{\partial C_{z,right}^{+}}{\partial d_x} = \frac{2\varepsilon_0 L_x L_y \phi \theta}{\left[F_z^{+} + B_z^{+} n_2^z + (A_z^{+} - L_x) n_1^z \right]^2} \tag{B.55}$$

$$\frac{\partial C^-_{z,right}}{\partial d_x} = -\frac{2\varepsilon_0 L_x L_y \phi \theta}{\left[F^-_z - B^-_z n^z_2 - (A^-_z - L_x)n^z_1\right]^2} \tag{B.56}$$

The terms useful for stiffness calculations are variations of capacitances and capacitance gradients. These are given by

$$\delta C^+_{x,up} = \frac{-2\varepsilon_0 L_y L_z}{\left[F^+_x + B^+_x n^x_2 + (A^+_x + L_y)n^x_1\right]^2} \delta \left[F^+_x + B^+_x n^x_2 + (A^+_x + L_y)n^x_1\right] \tag{B.57}$$

$$\delta C^-_{x,up} = \frac{-2\varepsilon_0 L_y L_z}{\left[F^-_x - B^-_x n^x_2 - (A^-_x + L_y)n^x_1\right]^2} \delta \left[F^-_x - B^-_x n^x_2 - (A^-_x + L_y)n^x_1\right] \tag{B.58}$$

$$\delta C^+_{x,down} = \frac{-2\varepsilon_0 L_y L_z}{\left[F^+_x + B^+_x n^x_2 + (A^+_x - L_y)n^x_1\right]^2} \delta \left[F^+_x + B^+_x n^x_2 + (A^+_x - L_y)n^x_1\right] \tag{B.59}$$

$$\delta C^-_{x,down} = \frac{-2\varepsilon_0 L_y L_z}{\left[F^-_x - B^-_x n^x_2 - (A^-_x - L_y)n^x_1\right]^2} \delta \left[F^-_x - B^-_x n^x_2 - (A^-_x - L_y)n^x_1\right] \tag{B.60}$$

Finally the last useful formulae for stiffness calculations are those of the type $\delta C'_i$. On the x-axis we have

$$\delta C^{+'}_{x,up} = \frac{-4\varepsilon_0 L_y L_z}{\left[F^+_x + B^+_x n^x_2 + (A^+_x + L_y)n^x_1\right]^3} \delta \left[F^+_x + B^+_x n^x_2 + (A^+_x + L_y)n^x_1\right] \tag{B.61}$$

$$\delta C^{-'}_{x,up} = \frac{4\varepsilon_0 L_y L_z}{\left[F^-_x - B^-_x n^x_2 - (A^-_x + L_y)n^x_1\right]^3} \delta \left[F^-_x - B^-_x n^x_2 - (A^-_x + L_y)n^x_1\right] \tag{B.62}$$

$$\delta C^{+'}_{x,down} = \frac{-4\varepsilon_0 L_y L_z}{\left[F^+_x + B^+_x n^x_2 + (A^+_x - L_y)n^x_1\right]^3} \delta \left[F^+_x + B^+_x n^x_2 + (A^+_x - L_y)n^x_1\right] \tag{B.63}$$

$$\delta C^{-'}_{x,down} = \frac{4\varepsilon_0 L_y L_z}{\left[F^-_x - B^-_x n^x_2 - (A^-_x - L_y)n^x_1\right]^3} \delta \left[F^-_x - B^-_x n^x_2 - (A^-_x - L_y)n^x_1\right] \tag{B.64}$$

On the y-axis the expressions are as follows:

$$\delta C^{+'}_{y,up} = \frac{4\varepsilon_0 L_x L_z(\phi + \psi)}{\left[F^+_y + A^+_y n^y_1 + (B^+_y + L_z)n^y_2\right]^3} \delta \left[F^+_y + A^+_y n^y_1 + (B^+_y + L_z)n^y_2\right] \tag{B.65}$$

$$\delta C^{-'}_{y,up} = -\frac{4\varepsilon_0 L_x L_z(\phi + \psi)}{\left[F^-_y - A^-_y n^y_1 - (B^-_y + L_z)n^y_2\right]^3} \delta \left[F^-_y - A^-_y n^y_1 - (B^-_y + L_z)n^y_2\right] \tag{B.66}$$

$$\delta C^{+'}_{y,down} = \frac{4\varepsilon_0 L_x L_z(\phi + \psi)}{\left[F^+_y + A^+_y n^y_1 + (B^+_y - L_z)n^y_2\right]^3} \delta \left[F^+_y + A^+_y n^y_1 + (B^+_y - L_z)n^y_2\right] \tag{B.67}$$

$$\delta C^{-'}_{y,right} = -\frac{4\varepsilon_0 L_x L_z(\phi + \psi)}{\left[F^-_y - A^-_y n^y_1 - (B^-_y - L_z)n^y_2\right]^3} \delta \left[F^-_y - A^-_y n^y_1 - (B^-_y - L_z)n^y_2\right] \tag{B.68}$$

And finally on the z-axis we have

$$\delta C^{+'}_{z,left} = -\frac{4\varepsilon_0 L_x L_y \phi \theta}{\left[F^+_z + B^+_z n^z_2 + (A^+_z + L_x)n^z_1\right]^3} \delta \left[F^+_z + B^+_z n^z_2 + (A^+_z + L_x)n^z_1\right] \tag{B.69}$$

$$\delta C_{z,left}^{-'} = \frac{4\varepsilon_0 L_x L_y \phi\theta}{\left[F_z^- - B_z^- n_2^z - (A_z^- + L_x)n_1^z\right]^3}\delta\left[F_z^- - B_z^- n_2^z - (A_z^- + L_x)n_1^z\right] \quad (B.70)$$

$$\delta C_{z,right}^{+'} = -\frac{4\varepsilon_0 L_x L_y \phi\theta}{\left[F_z^+ + B_z^+ n_2^z + (A_z^+ - L_x)n_1^z\right]^3}\delta\left[F_z^+ + B_z^+ n_2^z + (A_z^+ - L_x)n_1^z\right] \quad (B.71)$$

$$\delta C_{z,right}^{-'} = \frac{4\varepsilon_0 L_x L_y \phi\theta}{\left[F_z^- - B_z^- n_2^z - (A_z^- - L_x)n_1^z\right]^3}\delta\left[F_z^- - B_z^- n_2^z - (A_z^- - L_x)n_1^z\right] \quad (B.72)$$

where for the x, y and z axes we have

$$\delta\left[F_x^+ + B_x^+ n_2^x + (A_x^+ \pm L_y)n_1^x\right] = -\delta d_x \pm L_y(\delta\phi + \delta\psi) \quad (B.73)$$

$$\delta\left[F_x^- - B_x^- n_2^x - (A_x^- \pm L_y)n_1^x\right] = +\delta d_x \mp L_y(\delta\phi + \delta\psi) \quad (B.74)$$

$$\delta\left[F_y^+ + A_y^+ n_1^y + (B_y^+ \pm L_z)n_2^y\right] = -\delta d_y \pm L_z\delta\theta \quad (B.75)$$

$$\delta\left[F_y^- - A_y^- n_1^y - (B_y^- \pm L_z)n_2^y\right] = \delta d_y \mp L_z\delta\theta \quad (B.76)$$

$$\delta\left[F_z^+ + B_z^+ n_2^z + (A_z^+ \pm L_x)n_1^z\right] = -\delta d_z \quad (B.77)$$

$$\delta\left[F_z^- - B_z^- n_2^z - (A_z^- \pm L_x)n_1^z\right] = \delta d_z \quad (B.78)$$

Appendix B.1. *Capacitance as a position sensor.*

By measuring and combining capacitances along the different axis, we can obtain the position and attitude of the proof mass. The parameters $(d_x, d_y, d_z, \phi, \theta, \psi)$ are obtained by the following combination of capacitances,

$$(C_{z,r}^+ - C_{z,r}^-) + (C_{z,l}^+ - C_{z,l}^-) \simeq 8\varepsilon_0 L_x L_y \frac{d_z}{D_z^2} \quad (B.79)$$

$$(C_{z,r}^+ - C_{z,r}^-) - (C_{z,l}^+ - C_{z,l}^-) \simeq 8\varepsilon_0 \frac{L_x^2 L_y}{D_z^2}\theta\phi \quad (B.80)$$

$$(C_{x,up}^+ - C_{x,up}^-) + (C_{x,down}^+ - C_{x,down}^-) \simeq 8\varepsilon_0 L_z L_y \frac{d_x}{D_x^2} \quad (B.81)$$

$$(C_{x,up}^+ - C_{x,up}^-) - (C_{x,down}^+ - C_{x,down}^-) \simeq -8\varepsilon_0 L_y^2 L_z(\phi + \psi)\frac{1}{D_x^2} \quad (B.82)$$

$$(C_{y,up}^+ - C_{y,up}^-) + (C_{y,down}^+ - C_{y,down}^-) \simeq 8\varepsilon_0 L_x L_z \frac{d_y}{D_y^2} \quad (B.83)$$

$$(C_{y,up}^+ - C_{y,up}^-) - (C_{y,down}^+ - C_{y,down}^-) \simeq -8\varepsilon_0 L_x L_z^2\theta\frac{1}{D_y^2} \quad (B.84)$$

Appendix B.2. *Capacitances, capacitance derivatives and their variations*

For the special case in which the proof mass is in the equilibrium position, $\vec{0}$, with no translational and rotational offsets,

$$C_{x,up}^{\pm} = C_{x,down}^{\pm} = \frac{2\varepsilon_0 L_y L_z}{D_x} \tag{B.85}$$

$$C_{y,up}^{\pm} = C_{y,down}^{\pm} = \frac{2\varepsilon_0 L_x L_z}{D_y} \tag{B.86}$$

$$C_{z,left}^{\pm} = C_{z,right}^{\pm} = \frac{2\varepsilon_0 L_x L_y}{D_z} \tag{B.87}$$

$$\frac{\partial C_{x,up}^{\pm}}{\partial d_x} = \frac{\partial C_{x,down}^{\pm}}{\partial d_x} = \pm\frac{2\varepsilon_0 L_y L_z}{D_x^2} \tag{B.88}$$

$$\frac{\partial C_{y,up}^{\pm}}{\partial d_x} = \frac{\partial C_{y,down}^{\pm}}{\partial d_x} = \frac{\partial C_{z,left}^{\pm}}{\partial d_x} = \frac{\partial C_{z,right}^{\pm}}{\partial d_x} \approx 0 \tag{B.89}$$

$$\delta C_{x,up}^{\pm} = \mp\frac{2\varepsilon_0 L_y L_z}{D_x^2} \left[-\delta d_x + L_y(\delta\phi + \delta\psi)\right] \tag{B.90}$$

$$\delta C_{x,down}^{\pm} = \mp\frac{2\varepsilon_0 L_y L_z}{D_x^2} \left[-\delta d_x - L_y(\delta\phi + \delta\psi)\right] \tag{B.91}$$

$$\delta C_{y,up}^{\pm} = \mp\frac{2\varepsilon_0 L_x L_z}{D_y^2} \left[-\delta d_y + L_z\delta\theta\right] \tag{B.92}$$

$$\delta C_{y,down}^{\pm} = \mp\frac{2\varepsilon_0 L_x L_z}{D_y^2} \left[-\delta d_y - L_z\delta\theta\right] \tag{B.93}$$

$$\delta C_{z,left}^{\pm} = \delta C_{z,right}^{\pm} = \pm\frac{2\varepsilon_0 L_x L_y}{D_z^2}\delta d_z \tag{B.94}$$

$$\delta C_{x,up}^{\pm\,\prime} = \frac{-4\varepsilon_0 L_y L_z}{D_x^3} \left[-\delta d_x + L_y(\delta\phi + \delta\psi)\right] \tag{B.95}$$

$$\delta C_{x,down}^{\pm\,\prime} = \frac{-4\varepsilon_0 L_y L_z}{D_x^3} \left[-\delta d_x - L_y(\delta\phi + \delta\psi)\right] \tag{B.96}$$

$$\delta C_{y,up}^{\pm\,\prime} = \delta C_{y,down}^{\pm\,\prime} = \delta C_{z,left}^{\pm\,\prime} = \delta C_{z,right}^{\pm\,\prime} \approx 0 \tag{B.97}$$